CHEMISTRY OF MATERIALS

pubs.acs.org/cm Article

Dynamics of Hydroxyl Anions Promotes Lithium Ion Conduction in Antiperovskite Li_2OHCl

Fei Wang, Hayden A. Evans, Kwangnam Kim, Liang Yin, Yiliang Li, Ping-Chun Tsai, Jue Liu, Saul H. Lapidus, Craig M. Brown, Donald J. Siegel, and Yet-Ming Chiang*

Cite This: *Chem. Mater.* 2020, 32, 8481−8491 Read Online

ABSTRACT: Li_2OHCl is an exemplar of the antiperovskite family of ionic conductors, for which high ionic conductivities have been reported, but in which the atomic-level mechanism of ion migration is unclear. The stable phase is both crystallographically defective and disordered, having ∼1/3 of the Li sites vacant, while the presence of the OH^- anion introduces the possibility of rotational disorder that may be coupled to cation migration. Here, complementary experimental and computational methods are applied to understand the relationship between the crystal chemistry and ionic conductivity in Li_2OHCl, which undergoes an orthorhombic to cubic phase transition near 311 K (≈38 °C) and coincides with the more than a factor of 10 change in ionic conductivity (from 1.2 × 10^{-5}mS/cm at 37 °C to 1.4 × 10^{-3} mS/cm at 39 °C). X-ray and neutron experiments conducted over the temperature range 20−200 °C, including diffraction, quasi-elastic neutron scattering (QENS), the maximum entropy method (MEM) analysis, and *ab initio* molecular dynamics (AIMD) simulations, together show conclusively that the high lithium ion conductivity of cubic Li_2OHCl is correlated to "paddlewheel" rotation of the dynamic OH^- anion. The present results suggest that in antiperovskites and derivative structures a high cation vacancy concentration combined with the presence of disordered molecular anions can lead to high cation mobility.

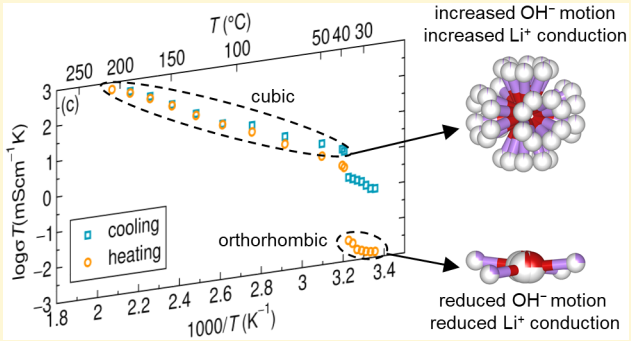

■ INTRODUCTION

Solid-state Li-ion conductors have received a great deal of attention in recent years for their promise in enabling batteries that have reduced flammability compared to current liquid electrolyte based Li-ion batteries and that can access higher energy density regimes available with lithium metal electrodes.[1,2] Among known families of solid-state electrolytes (SSE), antiperovskites (APs) with the formula X_3AB (where X is Li^+ or Na^+ and A and B are smaller and larger anions, respectively) have recently attracted interest for the high ionic conductivities reported in select compositions.[3−5] Like the well-known and extensively studied perovskite compounds,[6−8] flexibility in composition and phase afforded by ion substitution onto multiple lattice sites suggests broad latitude in tuning AP properties. Despite a growing number of studies of this structural class, many fundamental questions remain unanswered concerning the interrelationship between structure, disorder, and ion transport. Recent computational studies suggest that relative ion sizes, as captured by the Goldschmidt tolerance factor, affect structural stability in APs in a manner similar to that in perovskites and create disorder that is accompanied by a broadened distribution of lithium migration energies.[9] Another characteristic of APs is their ability to accommodate molecular anions, exemplified by the composition examined in this paper, Li_2OHCl, which has been of interest due to its high reported ionic conductivity at room temperature.[10]

Although earlier studies suggested the existence of the "ideal" composition Li_3OCl,[3,11,12] more recent work including this study has found that a single phase of the AP structure is obtained only when the composition approaches the formula Li_2OHCl.[13−15] In the idealized Li_3OCl phase, Zhang et al. proposed a lithium vacancy hopping mechanism and calculated the migration barrier to be 367 meV.[16] In contrast, Emly et al. proposed a migration mechanism involving coordinated motion of Li^+ interstitial dumbbells, created by a Frenkel mechanism, for which the computed energy barrier is one-half that for vacancy migration.[17]

In Li_2OHCl (vs Li_3OCl), two of the six Li^+ ions that comprise the vertices of the Li_6O pseudo-octahedra are missing, and the O^{2-} ion residing at the center of the

Received: June 21, 2020
Revised: September 1, 2020
Published: September 1, 2020

https://dx.doi.org/10.1021/acs.chemmater.0c02602
Chem. Mater. 2020, 32, 8481−8491

pseudo-octahedron is replaced with an OH^- anion. At ≈310 K, Li_2OHCl undergoes an orthorhombic-to-cubic phase transition,[10,18] which, as results presented later confirm, coincides with about a factor of 10 increase in ionic conductivity.[13,19,20] Currently, the Li^+ conduction mechanism in the highly conducting cubic phase remains a topic of interest, in part because of the complexities imparted by the dynamic rotation of OH^- anions and their potential interplay with Li^+ migration. Simulations by Howard et al. showed that OH^- bond orientations participate in gating the Li^+ motion.[21] NMR experiments and simulations by Dawson et al. showed that the H rotates around the O atom and that the Li ions have long-range mobility.[22] Studies by Song et al. have argued for correlated motion between OH^- and Li^+ through simulations on a ordered cubic structure with ordered arrangements of Li and H.[14,19] Experimentally, the structural details of light elements in Li_2OHCl have not been clear from X-ray diffraction (XRD) alone, but Hanghofer et al.[13] recently used neutron diffraction to characterize the H and Li^+ positions and found a complex situation in the cubic polymorph complicated by phase decomposition, while the distributions were determined to a greater certainty in the low-temperature orthorhombic polymorphs.

The present study aims to further elucidate the atomic structure of Li_2OHCl, the relationship between structure, Li^+ site disorder, and rotational dynamics of the OH^- anions, and whether or how the combined effects of these features may flatten the energy landscape associated with cation migration, resulting in enhanced Li-ion conductivity. A combination of experimental and theoretical techniques is used to demonstrate that Li^+ ion conduction in cubic Li_2OHCl occurs via a "paddlewheel" mechanism[23] coupled to rotational disorder of the OH^- anions. This mechanism, in turn, suggests design criteria for obtaining high ionic conductivity in other APs.

■ EXPERIMENTAL METHODS

Materials Synthesis. To avoid the uncontrolled influence of moisture, all of the following procedures, from mixing of starting materials to measurement of conductivity, were performed in argon- or helium-filled gloveboxes with water and oxygen content below 1 ppm (1 μg/g). Anhydrous LiOH (Sigma-Aldrich, anhydrous, 99.5%) or LiOD (Cambridge Isotope Laboratories, 99.5%) and LiCl (Sigma-Aldrich, anhydrous, 99.9%) were mixed in a molar ratio of 1.05:1, ground by hand using an agate mortar and pestle for 10 min, and homogenized in the molten state in alumina crucibles at 593 K (≈320 °C) for 2 h. The melt was then poured into a Teflon die and allowed to cool.[10,23] The solidified sample was then ground in an agate mortar and subsequently ball-milled for 10 min in a SPEX SamplePrep Mixer/Mill 8000 M by using a steel jar and steel milling balls. To determine whether the antiperovskite phase had been obtained, powder X-ray diffraction (PXRD) was performed by using a PANalytical X'Pert Pro multipurpose diffractometer equipped with a Cu Kα radiation source and an X'Celerator detector. All temperature-dependent synchrotron X-ray (SXRD) and neutron powder diffraction (NPD) experiments used the same lot of as-prepared Li_2ODCl powder. Different batches of Li_2OHCl powders were used for the temperature-dependent PXRD and total scattering experiments (PDF).

Electrical Conductivity Measurements. Dense pellets of 1 mm diameter and ≈2 mm thickness were obtained by pressing the powders at 393 K (120 °C) under 500 MPa uniaxial pressure in steel dies. Gold electrodes were sputtered on both faces of the pellet, forming ion-blocking electrodes. Impedance spectroscopy (IS) was performed over the frequency range 1 Hz−10 MHz and over a temperature range of 298−493 K (25−220 °C) by using commercial instrumentation (Probostat, manufactured by NORECS, Norway).

Powder Neutron Diffraction. Measurements were performed on a 0.6 g sample of Li_2ODCl powder at the National Institute of Standards and Technology Center for Neutron Research (NCNR). Data were collected at the high-resolution neutron powder diffractometer, BT-1, utilizing a Cu(311) monochromator with an in-pile 60 ft collimator, corresponding to a neutron wavelength of 1.5400 Å. The sample was loaded into a vanadium sample can in a He environment glovebox and sealed with a soldered lead O-ring onto a copper heating block. After the sample was mounted onto a bottom-loaded closed cycle refrigerator (CCR), the same was measured at 303 and 553 K for a sufficient time to be able to perform high quality Rietveld refinements. The measured temperatures were chosen to be above and below the known orthorhombic-to-cubic phase transition near 313 K (40 °C).[10] The room temperature powder diffraction of Li_2OHCl was also measured at POWGEN of Oak Ridge National Laboratory.

Quasi-Elastic Neutron Scattering. Measurements were performed on a 0.5 g sample of Li_2OHCl powder at the NCNR. Data were collected on the high-flux back spectrometer (HFBS) instrument. Inside a He glovebox, the sample was uniformly dispersed and sandwiched in an aluminum foil sheet that formed an annulus inside a cylindrical sample container. The aluminum sample container was then sealed with lead, removed from the glovebox, and loaded into a top loading closed cycle refrigerator (CCR). The fixed window scans, which are measurements of scattering vector (Q)-dependent elastic intensity vs temperature while the Doppler drive is stationary, were recorded every minute on heating, with an incident wavelength of 6.27 Å.

Neutron Data Analysis. NPD data were analyzed by using the TOPAS software suite.[25] Initial Pawley refinements were conducted to determine lattice parameters and peak shapes.[26] No reflections from LiCl were observed in the Li_2ODCl sample tested. The Dysnomia software suite was used for maximum entropy method (MEM) analysis.[27] Structural models of Li_2ODCl at 303 and 553 K were initially Rietveld-refined (between 3° and 140°) in Rietan.[28] Dysnomia was used to reconstruct the MEM scattering density for 48 × 48 × 48 voxels. The combined negative and positive coherent neutron scattering lengths for each element (Li = −1.90 fm, D = 6.671 fm, O = 5.803 fm, and Cl = 9.577 fm) were used. Following the preliminary Rietveld refinement, multiple iterations of total pattern fitting in Rietan, followed by MEM analysis in Dysnomia, were used to produce the final optimized MEM model using a Lagrangian multiplier (λ) factor of 37. The MEM and Rietveld structural models were visualized by using the VESTA software suite.[29]

Synchrotron X-ray Diffraction. High-resolution synchrotron X-ray powder diffraction (SXRD) data were collected at the 11-BM beamline at the Advanced Photon Source (APS) of Argonne National Laboratory with a wavelength of 0.457926 Å. The Li_2ODCl powder sample was loaded in 1 mm diameter quartz capillaries in an Ar-filled glovebox and sealed with epoxy. Data were collected at room temperature and 373 K (100 °C). Structures were refined by using the Rietveld method as implemented in the TOPAS software package (Bruker-AXS, version 6).

Synchrotron X-ray total scattering data were collected at beamline 11-ID-B at the APS, ANL. The rapid-acquisition pair distribution function (PDF) method was used with an X-ray energy of 86.7 k eV (λ = 0.1432 Å). A PerkinElmer amorphous Si two-dimensional image-plate detector (2048 × 2048 pixels and 200 × 200 μm pixel size) was used at a distance of ≈250 mm. The Li_2ODCl powder sample was loaded in 1.1 mm diameter Kapton capillaries in an Ar-filled glovebox and sealed with epoxy. Data were collected at multiple temperatures (100, 150, 200, 250, 300, 310, 320, 350, and 370 K). The two-dimensional data were converted to one-dimensional XRD data by using the GSAS-II software.[30] PDF results data were obtained from Fourier transformation of the background and Compton scattering corrected total data $S(Q)$ in xPDFsuite software over a Q range of 0.1−20 $Å^{-1}$. Fitting of the PDF data sets was performed by using the PDFgui software suite.[31]

***Ab Initio* Molecular Dynamics Simulations.** *Ab initio* molecular dynamics (AIMD) simulations were performed by using the Vienna

https://dx.doi.org/10.1021/acs.chemmater.0c02602
Chem. Mater. 2020, 32, 8481−8491

ab initio Simulation Package (VASP).[32] The Perdew–Burke–Ernzerhof (PBE)[33] exchange-correlation functional was used in combination with the projector augmented wave (PAW) method.[34,35] The following valence electron configurations were adopted: $1s^1$ for H, $2s^1$ for Li, $2s^22p^4$ for O, and $3s^23p^5$ for Cl. The plane-wave basis included functions with kinetic energies up to 520 eV. AIMD simulations were conducted by using the Verlet algorithm and the NVT ensemble with a Nosé–Hoover thermostat. Trajectory data were collected over 100 ps, after an initial 2 ps equilibration period. A time step of 1 fs was used for all AIMD simulations. AIMD was performed on the orthorhombic and cubic variants of Li_2OHCl. The simulation cell for the orthorhombic system was constructed from a 2 × 2 × 3 replication (240 atoms) of the orthorhombic unit cell. Simulations on the cubic phase were performed using a 3 × 3 × 3 replication (135 atoms) of the cubic unit cell. *K*-point sampling for both systems was performed by using a single *k*-point located at Γ. Experimentally determined lattice constants for the orthorhombic (a = 7.756 Å, b = 7.990 Å, and c = 3.823 Å at 303 K) and cubic (a = 3.944 Å at 553 K) phases were adopted for the AIMD calculations; the same lattice constants were used in the MEM analysis. Note that the computed lattice constants are a = 7.934 Å, b = 8.116 Å, and c = 3.786 Å for the orthorhombic phase and a = 3.974 Å for the cubic phase, close to the experimental values.

The relative mobilities of Li, O, H, and Cl ions were characterized by using mean-squared displacement (MSD) data extracted from the AIMD trajectories of atoms at position, **r**, and time, t, as

$$\mathrm{MSD} = \langle[\mathbf{r}(t + t_0) - \mathbf{r}(t_0)]^2\rangle$$

where t_0 is the initial time, and the angled bracket represents an average over time and over all atoms of the species in question. The positional probability densities were evaluated by subdividing the supercell into a grid of 0.25 × 0.25 × 0.25 $Å^3$ cubes. Position densities for a given cell were determined from the number of time steps for which each mesh was occupied by an atom.[36]

■ RESULTS AND DISCUSSION

Variable-temperature PXRD measurements were performed to investigate the temperature-dependent structural and compositional changes in Li_2OHCl. It was observed that Li_2OHCl undergoes an orthorhombic to cubic phase transition near 311 K (≈38 °C) (Figures 1a and 1b), which coincides with the more than factor of 10 change in ionic conductivity (from 1.2 × 10^{-5} mS/cm at 37 °C to 1.4 × 10^{-3} mS/cm at 39 °C, Figure 1c and Figure S1). The appearance of an ionic conductivity increase concurrent with a phase transition from orthorhombic to cubic phase is consistent with previous work,[19,20] although the magnitude of the change differs between studies. On the basis of recent results showing that the electronic conductivity is ∼10^{-11} S/cm in the same compound,[20] we assume an ionic transference number of unity. As shown in Figures 1a and 1b, the diffraction pattern of Li_2OHCl at 298 K (≈25 °C) shows orthorhombic splitting of reflections between 30° and 35° in the scattering angle (2θ) (for Cu Kα), which collapse to a single reflection upon heating and transformation to the cubic phase and then return upon cooling.[18] Upon cooling through the phase transition, the conductivity decreases abruptly by about a factor of 10 at the same transition temperature. For both the orthorhombic and cubic phases, a straight-line fit to the heating data in Figure 1c (i.e., assuming Arrhenius behavior) shows a somewhat lower activation energy for the cubic phase (E_a = 552 meV) than the orthorhombic phase (E_a = 640 meV). While the cubic phase clearly exhibits higher conductivity and shows approximately the same conductivity values upon heating and cooling, there is a larger hysteresis in the conductivity of the orthorhombic phase between the first heating and first cooling. The temperature at which the orthorhombic–cubic transition occurs does not change noticeably upon heating or cooling. We attribute the conductivity hysteresis to extrinsic factors such as changes in microstructure or grain boundary resistance,[37] given that the sample approaches the melting point of the compound at the upper temperature range of the conductivity sweep (T_m ≈ 573 K, measured in this work using differential scanning calorimetry, Figure S2).

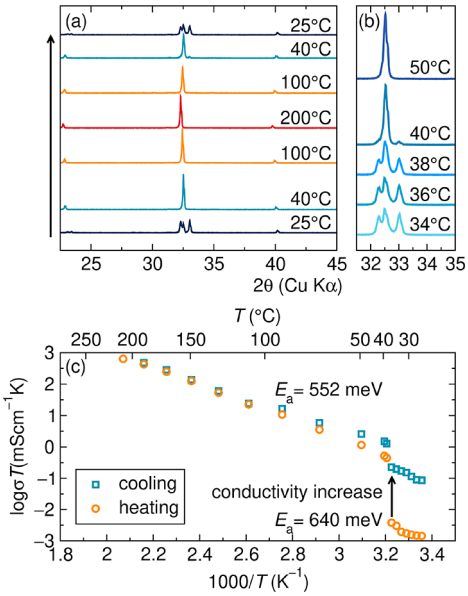

Figure 1. (a, b) Temperature-dependent PXRD patterns of the as-prepared Li_2OHCl upon heating and cooling through the orthorhombic–cubic transition. (c) Arrhenius plot of log(σT) vs 1/T for Li_2OHCl, showing a discontinuous change in conductivity of ≈10^2 during heating and ≈10 upon cooling through the orthorhombic–cubic transition temperature. Activation energies (assuming Arrhenius behavior) were obtained from the heating data set above and below the discontinuous change in ionic conductivity.

To understand the abrupt change in ionic conductivity associated with the phase transformation in more detail, high quality SXRD and NPD measurements were performed on the same sample batch of Li_2ODCl below and above the phase transition temperature. It is assumed that the behavior of the deuterated version is similar to that of the protiated variant. The detailed refinements of both SXRD and NPD data, as well as the refined structure of the cubic phase, are shown in Figure 2. For the SXRD refinements, the OD^- anion was modeled as a rigid body (O–D distance of 0.958 Å) and replicated by symmetry with an occupancy commensurate with the chemical formula Li_2ODCl. Rietveld refinement of the SXRD data of Li_2ODCl at 373 K (Figure 2a) identifies three resolvable phases. This includes phase "a" and phase "b", which are two variants of the *Pm*-3*m* structure, and a minor LiCl impurity (shown in more detail in Figure S3). According to the Rietveld refinement, 80 mass % of the material is composed of the larger unit cell cubic phase, phase "a", with lattice parameter of 3.91796(1) Å, and 15 mass % is attributed to the smaller unit cell cubic phase, phase "b", with lattice parameter of 3.90937(1) Å. LiCl accounts for the remaining 5 mass % of the sample. The difference between phase "a" and phase "b" is most likely differing amounts of Cl^-, Li^+, and OD^-, which we are not able to confidently resolve with the X-ray data. It is unclear whether this is a bulk representation of the sample, for example, reflecting solid–solid immiscibility of two defective

https://dx.doi.org/10.1021/acs.chemmater.0c02602
Chem. Mater. 2020, 32, 8481–8491

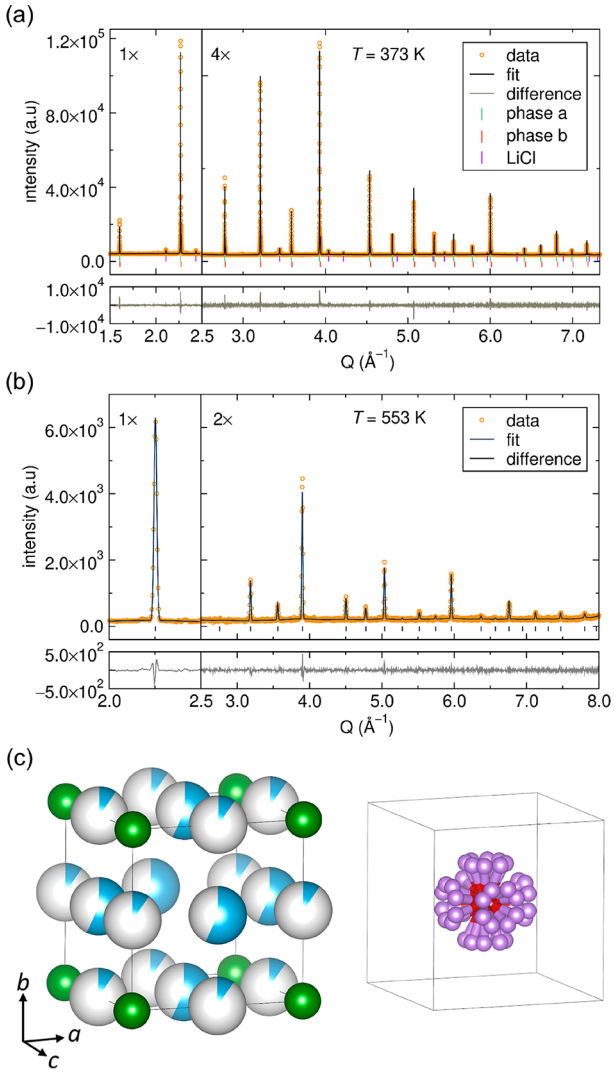

Figure 2. (a) Rietveld refinement of Li_2ODCl at 373 K [SXRD APS, 11-BM]. There is a major phase of Li_2OHCl (phase "a" ≈ 80 mass %) and a minor phase with a smaller unit cell (phase "b" ≈ 15 mass %). A LiCl impurity also exists (≈ 5 mass %). Li_2OHCl phase "a": space group *Pm*-3*m*, $a = b = c = 3.91796(1)$ Å, $V = 60.142(1)$ Å^3. Li_2OHCl phase "b": space group *Pm*-3*m*, $a = b = c = 3.90937(1)$ Å, $V = 59.748(1)$ Å^3. LiCl: space group *Fm*-3*m*, $a = b = c = 5.16088(5)$ Å, $V = 137.458(4)$ Å^3. Goodness of fit parameters: $R_p = 9.99\%$, $R_{wp} = 14.02\%$. Values in parentheses indicate one standard deviation. (b) Rietveld refinement of Li_2ODCl at 553 K [NPD NCNR, BT-1], space group *Pm*-3*m*, $a = b = c = 3.94374(8)$ Å, $V = 61.337(4)$ Å^3. Goodness of fit parameters: $R_p = 5.93\%$, $R_{wp} = 7.07\%$. (c) Structure from Rietveld refinement for Li_2ODCl at 553 K separated into two subfigures. Left: position of chloride and lithium ions. Right: disordered OD^- anion (both O and D atoms are split over general 48n positions, but D is illustrated with full spheres/occupancy in the figure for clarity). Atom legend: lithium, blue; chlorine, green; oxygen, red; deuterium, light purple.

antiperovskite compositions, or whether there are composition variations with the sample. This could also be a result of the relatively few particles of the sample that were exposed to X-rays, as potential variations in the powder within the capillary were not measured.

For Rietveld refinements of the NPD results (Figure 2b), a single cubic phase (*Pm*-3*m*, $a = b = c = 3.94374(8)$ Å) was refined where the OD^- anion was modeled as a rigid body (O−D distance of 0.958 Å) and replicated by symmetry with an occupancy commensurate with the chemical formula Li_2ODCl. No site mixing on the Cl site was evident, as it was reliably refined to full occupancy. The two lithium cation locations have site multiplicities of 3, with a maximum combined crystallographic occupancy of 0.667 (to achieve charge neutrality for the chemical formula Li_2ODCl) and were therefore refined with a constraint limiting their combined occupancy to 0.667. The primary lithium site is at (0.5, 0.5, 0) and refined to 85% of the total lithium occupancy. A secondary site, an edge site at (0.5, 0, 0), was refined to have 15% of the total lithium occupancy. The lithium occupancy of this interstitial edge site has not been reported in prior studies; it is presumed here that lithium occupancy of the edge site is stabilized by the one-third concentration of lithium vacancies in Li_2OHCl. A conduction pathway that proceeds from the cube face Li site through the edge site to another cube face site could therefore be a possibility, in addition to direct hops between the normally occupied face sites. Note that the interstitial edge site is distinct from the interstitial dumbbell defects proposed by Emly et al.[17] in vacancy-free Li_3OCl; in that case the Li−Li dumbbell is centered on the face Li sites and oriented along the cube edge of the unit cell. As for the OD^- anion, Rietveld refinement of the NPD data suggests that the O atom of the OD^- anion prefers to be placed at the center of the unit cell with D atoms pointing outward (Figure 2c). Notably, the D has eight coplanar orientations, with the occupied planes being parallel to the cube faces. The large number of configurations available in the cubic phase is in sharp contrast to the more limited configurations available in the low-temperature orthorhombic structure, discussed below. The rotation dynamics of the OD^- anion are strongly dependent on temperature/phase, with the cubic phase having a 3-dimensional distribution of D positions around the O atom (Figure 2c), whereas the orthorhombic phase has an almost 2-dimensional distribution (discussed below).

A maximum entropy method (MEM) analysis of the NPD data was utilized to establish the possible lithium conduction pathways and to provide a more holistic depiction of the OD^- disorder. MEM analysis fits models of neutron scattering density instead of chemical species (as in a Rietveld refinement) and is a useful technique where chemical disorder, as well as positive and negative neutron scattering contrast, exists. Li_2ODCl is a prime candidate in this respect, as it has disordered Li^+ cation and OD^- anion sites as well as neutron scattering contrast (lithium has a negative neutron cross section, and deuterium, chlorine, and oxygen have a positive neutron cross section).

The MEM analysis for cubic Li_2ODCl at 553 K is shown in Figure 3, separated into positive (yellow) and negative (blue) scattering densities. The density distribution for Li resolves at not only the anticipated position at (0.5, 0.5, 0) but also the partially occupied edge sites at (0.5, 0, 0). Because of the dynamic disorder of the OD^- anion, the relative positions of oxygen and deuterium cannot be resolved. The result nonetheless shows that in the cubic structure the distorted "ball" of OD^- density is highly localized in the center of the unit cell even at 553 K. With respect to the ion migration pathway at elevated temperature, it can be concluded that while Li-ion translational motion occurs by consecutive hops between closely spaced sites of comparatively low occupancy, D^+ motion is limited to rotation around the O, without longer-range hops between body-centered sites, which is in good

https://dx.doi.org/10.1021/acs.chemmater.0c02602
Chem. Mater. 2020, 32, 8481−8491

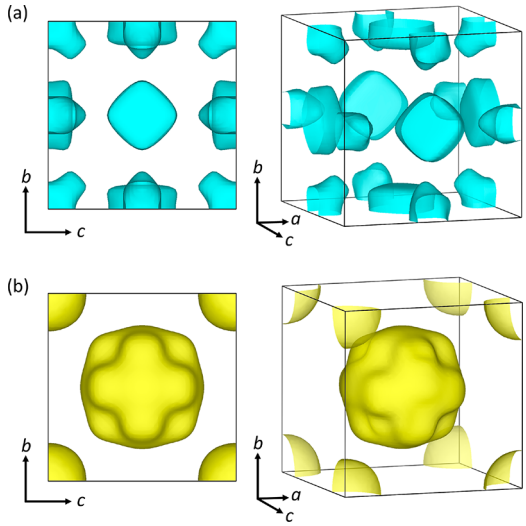

Figure 3. Maximum entropy method (MEM) constructed densities for neutron scattering data of cubic Li_2ODCl at 553 K. Negative density (corresponding to lithium) is displayed with blue, and positive density (corresponding to Cl, O, and D) is displayed with yellow. (a) Negative density, where both primary and secondary lithium sites can be seen at the faces and edges of the unit cell, respectively. (b) Positive density, where the chloride positions are seen at the corners of the unit cell, and the disordered OD^- anion appears as a lobed sphere consistent with *Pm-3m*, symmetry. The isosurface level was set at 0.1 units of neutron scattering length for each subfigure.

agreement with previously reported ^2H NMR results by Dawson et al.,[22] and indicates an absence of significant proton conductivity.

Room temperature SXRD of Li_2ODCl and NPD of Li_2ODCl were refined to an orthorhombic defective AP structure (Figures 4a and 4b, respectively). The detailed structure of orthorhombic Li_2ODCl is illustrated in Figure 4c. The high resolution provided by 11-BM reveals that the 303 K data (orthorhombic phase) is considerably more complex than the 373 K data (cubic phase), as two variants of the *Pban* structure alongside the LiCl impurity are insufficient to adequately model the data (if one is to assume that each of the two cubic phases transitions to respective orthorhombic phases). However, three phases excluding the LiCl impurity appear better suited to fit the data (Figure S4), but the exact nature of these individual phases cannot be determined conclusively.

A Rietveld model containing a single phase of a disordered rigid body OD^- anion (O−D distance of 0.958 Å) with occupancy commensurate with the formula Li_2ODCl was refined against the neutron data, shown in Figure 4b. The orthorhombic symmetry of Li_2ODCl was further confirmed with the following unit cell parameters (at 303 K): a = 7.7578(4) Å, b = 7.9963(3) Å, and c = 3.8254(2) Å, whose space group symmetry is *Pban* (No. 50) (also confirmed from data collected at Oak Ridge National Laboratory, Figure S5). The detailed structure of Li_2ODCl is illustrated in Figure 4c. The O atom locations were simplified from initial simulated annealing determined locations and placed on the b = 0.25 coordinate. The model contains six separate lithium positions determined via simulated annealing. Hereafter we will assume that D and H have the same positions when in the same structure. It is clear that O, H, and Li all have positional disorder. The H-occupied sites are close to the oxygen positions and split into four possible positions. However, there

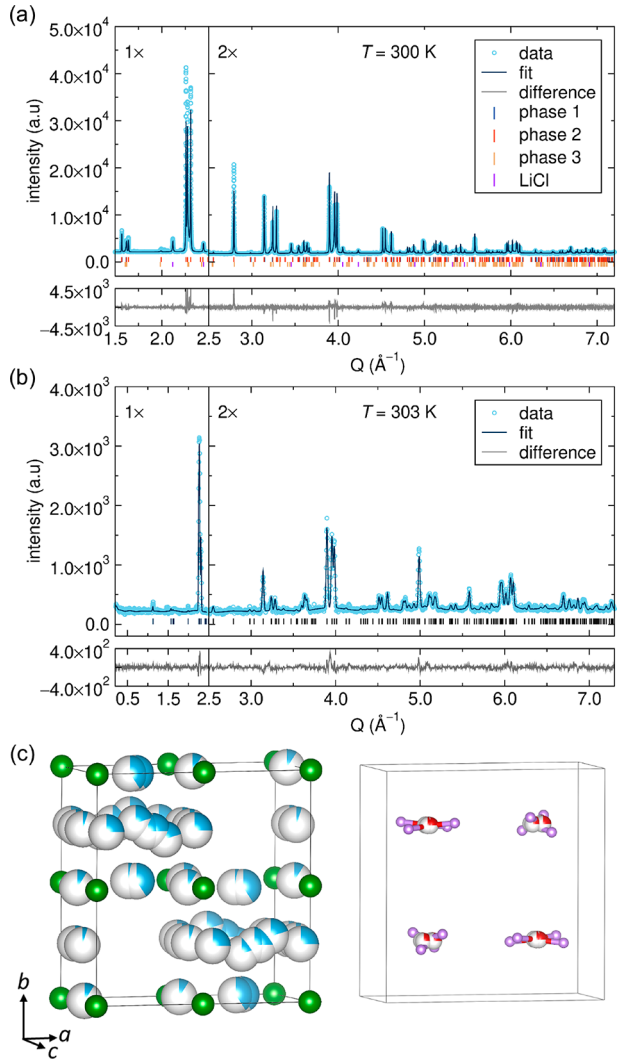

Figure 4. (a) Rietveld refinement of Li_2OHCl at 300 K [SXRD APS, 11-BM]. Phase 1: space group *Pban*, a = 7.7625(3), b = 7.9874(3), c = 3.8257(3) Å, V = 237.20(1) Å^3. Phase 2: space group *Pban*, a = 7.7527(1), b = 7.9991(1), c = 3.8265(1) Å, V = 237.30(1) Å^3. Phase 3: space group *Pban*, a = 7.794(1), b = 7.820(1), c = 3.8200(6) Å, V = 235.90(1) Å^3. LiCl: space group *Fm-3m*, $a = b = c$ = 5.14242(8) Å, V = 135.989(7) Å^3. Goodness of fit parameters: R_p = 14.26%, R_{wp} = 18.68%. LiCl ≈ 5 mass %. Values in parentheses indicate one standard deviation. (b) Rietveld refinement of Li_2ODCl at 303 K [NPD NCNR, BT-1], space group *Pban*, a = 7.7578(4), b = 7.9963(3), c = 3.8254(2) Å, V = 237.31(2) Å^3. Goodness of fit parameters: R_p = 8.38%, R_{wp} = 10.32%. Values in parentheses indicate one standard deviation. (c) Structure derived from Rietveld refinement for Li_2ODCl at 303 K, separated into two subfigures for clarity. Left: position of chloride and disordered lithium ions. Right: disordered OD^- anions (both O and D atoms are split over 8m sites, but D is depicted with full occupancy/sphere for clarity). Atom legend: lithium, blue; chlorine, green; oxygen, red; deuterium, light purple.

are two different arrangements of H around O, depending on the Li coordination. In one of these, the four H positions are almost in the same plane but are not coplanar with any of the principal axes, a, b, or c. We expect that each of these H positions is preferentially oriented in the direction of a Li vacancy, where there is reduced like-charge electrostatic repulsion. Our results differ from the NPD results of Hanghofer et al.,[13] in which no O disorder and only two H positions were shown. As shown in Figure 5, the MEM

https://dx.doi.org/10.1021/acs.chemmater.0c02602
Chem. Mater. 2020, 32, 8481−8491

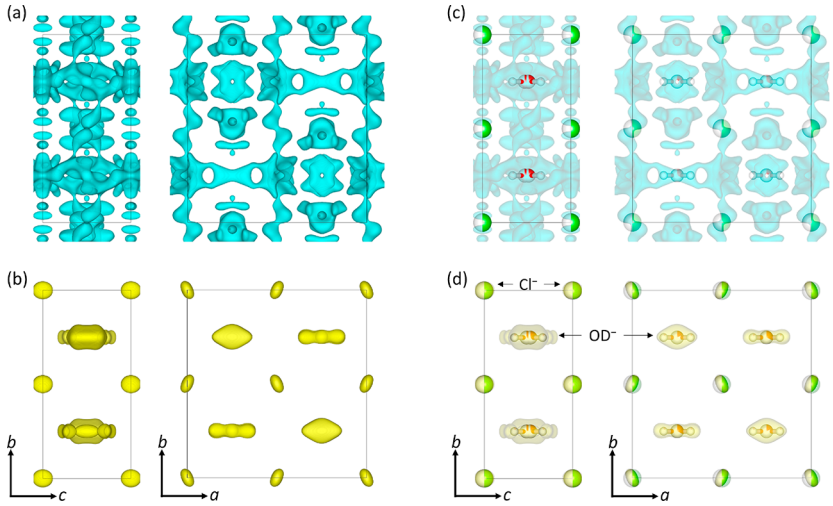

Figure 5. MEM constructed densities for neutron scattering data of orthorhombic Li_2ODCl at 303 K. Negative density (Li) is displayed as blue, and positive density (Cl, O, D) is displayed as yellow. (a) Negative density, where the disordered negative density from Li^+ ions clearly contrasts with the more localized positive density shown in the last two panels of the figure. (b) Negative density overlaid with localized Cl^- and OD^- positions. (c) Positive density, showing the well-resolved chloride and disordered OD^- positions. (d) Positive density overlaid with chloride and OD^- positions (labeled, where positions also apply to panel b). The isosurface level was set at 0.1 units of neutron scattering length for each subfigure.

reconstructed density of Li_2ODCl at 303 K illustrates localized Cl positions, reduced disorder of the OD^- relative to the high temperature cubic phase, and a complicated labyrinth of Li density. No easy path for Li-ion conduction is indicated, which may account for the higher activation energy and lower conductivity in the orthorhombic phase (Figure 1c). However, as the neutron diffraction sample size was much larger than the X-ray analyzed sample, it is understood that this is an average picture of potentially numerous similar orthorhombic phases that could form upon cooling from the cubic regime. The difference between our results and those of Hanghofer et al.[13] may reflect differences in phase content originating from differences in cooling procedure, where we utilized a more rapid quench than in their case.

X-ray total scattering measurements were taken to verify possible local short-range deviation from the average structure of Li_2OHCl. Measurements were conducted over a wide temperature range from 100 to 370 K and transformed to the PDF function (Figure S5) and fit above the orthorhombic-to-cubic phase transition. As can be seen in Figure 6a, an excellent fit is obtained at both short- and long-range order by refining the *Pm*-3*m* average structure alongside a LiCl impurity against the 320 K (≈47 °C) data set. To adequately fit the data, a much larger LiCl impurity amount relative to the synchrotron X-ray sample had to be included in the fit, attributed to sample degradation possibly related to inadvertent air exposure. Other data sets in the cubic temperature range (310 and 350 K) were examined and found to have a similar amount of LiCl. The refinement of the 320 K data set confirms that there is no major positional deviation of the O and Cl atoms (as the X-ray measurements are more sensitive to these elements relative to Li and H) in short range from what is expected from the SXRD and NPD determined average structure. Comparing the low temperature to the higher temperature data (Figure S6), the most obvious variation corresponds to the gradual broadening of the anion−anion correlations as temperature increases, as is expected from the increased thermal motion of the atoms and the increased rotational disorder of the hydroxide anion.

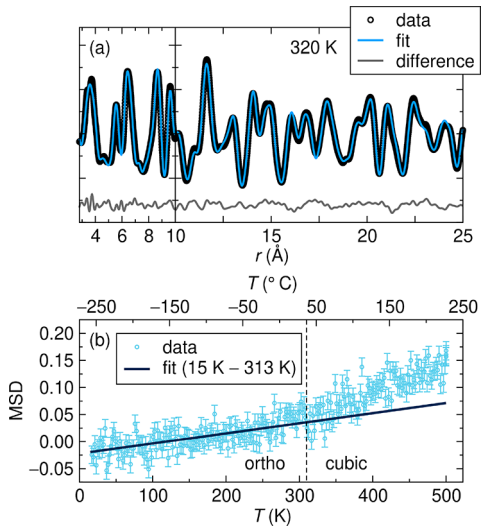

Figure 6. X-ray pair distribution function (PDF) of Li_2OHCl in the cubic regime (320 K). Shown are the two separate fits performed between 2.5 and 10 Å and between 10 and 25 Å. The fit to each data region contains two phases: Li_2OHCl (83 mass %); *Pm*-3*m*, $a = b = c = 3.918$ Å, short-range; $a = b = c = 3.915$ Å, long-range and LiCl (17 mass %) *Fm*-3*m* $a = b = c = 5.146$ Å, short-range; $a = b = c = 5.157$ Å, long-range. The larger than expected mass percent of LiCl relative to the synchrotron X-ray sample is likely due to sample degradation from inadvertent air exposure. (b) Fixed window scan between 15 and 500 K of Li_2OHCl [NCNR, HFBS]. There is an increase in MSD of the OH^- ion above the phase transition temperature near ≈313 K. These changes in slope between the orthorhombic (<313 K) and cubic (>313 K) phase regions are indicative of increased dynamic motion of OH^-. The MSD results are given in units of $Å^2$, with each value equal to $\langle u\rangle^2(T) - \langle u\rangle^2$ (T = base). Error bars represent ± one standard deviation.

The difference in atom dynamics between the cubic and orthorhombic phases was probed by using quasi-elastic neutron scattering (QENS). Figure 6b shows the MSD of the OH^- ion (which contains H, the element with the largest

https://dx.doi.org/10.1021/acs.chemmater.0c02602
Chem. Mater. 2020, 32, 8481−8491

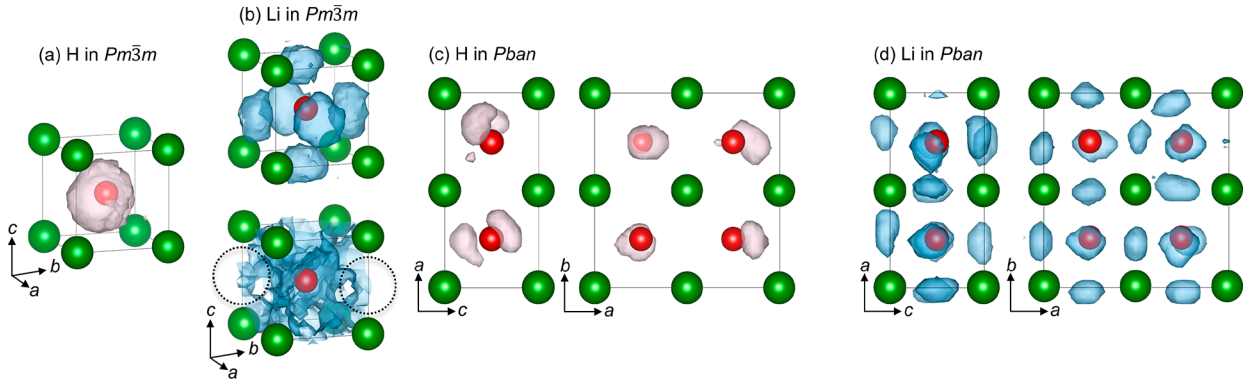

Figure 7. Ionic probability densities evaluated from 100 ps AIMD trajectories: (a) H (beige isosurface) and (b) Li with different isosurface levels (light blue isosurface) in cubic Li_2OHCl (space group *Pm*-3*m*) at 1000 K, and (c) H (beige isosurface) and (d) Li (blue isosurface) in orthorhombic Li_2OHCl (space group *Pban*) at 300 K. Orange circles in (b) indicate examples of the edge site between Cl atoms. Atom legend: chlorine = green; oxygen = red. The isosurface level was set at 0.003 1/bohr^3 for each subfigure.

incoherent scattering cross section in the sample), obtained from fixed window scans. The MSD is determined from fitting the elastic scattering intensity as a function of momentum transfer, *Q*. There is a clear increase in MSD of the OH^- anion from its linear harmonic behavior at ≈313 K (≈40 °C), coincident with the sharp rise in ionic conductivity shown in Figure 1c. The increased dynamic motion of the OH^- anion in the cubic phase is clearly correlated to the increased mobility of lithium, as we discuss below based on AIMD data. To summarize the difference in OH^- dynamics between the two phases based on the experimental data, upon cooling from the cubic into the orthorhombic phase, the movement of the OH^- anions slows down. This is evident from the QENS result in Figure 6b. The different proton movement modes were reported by Song et al.,[14] who showed four dynamic modes of 1 H in NMR, which are rigid at <−40 °C, small-angle rotation at −40 °C < T < −10 °C, onset of large angle rotation at −10 °C < T < 40 °C, and still anisotropic at T > 40 °C. Our MSD measurement covers the same temperature range but does not clearly indicate four different dynamic regions. The difference in observation is to be expected as the time scale for neutron scattering is in the nanosecond regime, several orders of magnitude faster than NMR. A modeling of dynamic QENS components (not measured here) would be required to determine the most appropriate reorientational model observable on the time scales of the HFBS instrument.

As shown in the MEM analysis of the orthorhombic phase, the density distribution of the OH^- anion is limited to a narrow 2D plane, contrasting with less-constrained the lobed sphere of density in the cubic phase. Consequently, in the orthorhombic phase, the Li^+ ions are statistically distributed among the available sites contributing to the reduced symmetry. No clear Li^+ ion conduction pathway could be easily deduced, consistent with the higher activation energy and lower conductivity in the orthorhombic phase. In the cubic phase, there is greater dynamic disorder of the OH^- anion, which is found to be localized to the body center of the unit cell. From the comparison between the cubic and orthorhombic phases, we can conclude that positional disorder of OH^- plays a major role in determining structure and Li^+ mobility. Its high rotational freedom at higher temperature, associated with increased configurational entropy, stabilizes the higher symmetry cubic phase. This in turn facilitates Li^+ hopping between face-centered and edge sites.

AIMD simulations were performed to investigate Li^+ and H^+ dynamics in orthorhombic and cubic Li_2OHCl. Figure 7 presents ionic probability density plots for H and Li, which were extracted from the AIMD trajectories. Consistent with the MEM analysis (Figures 3 and 5), the calculated probability density reveals that H atoms rotate freely around O atoms in the cubic structure (Figure 7a), whereas H is confined to the *ac* plane in the orthorhombic structure (Figure 7c). The top panel of Figure 7b, corresponding to a larger isosurface value for the probability density, shows that Li^+ displacements in the cubic phase result in a distribution centered on the Li sublattice sites at the vertices of the Li pseudo-octahedron (i.e., face centers of the cubic unit cell). Moreover, if one plots a smaller value of the probability isosurface (down panel, Figure 7b), the Li occupancy of the edge site becomes apparent. In total, the occupancy probabilities for Li generated from AIMD are in good agreement with the MEM analysis (Figure 3a).

The MSD for Li^+ and H^+ was calculated for cubic and orthorhombic Li_2OHCl at a common temperature of 550 K (where the orthorhombic phase is thermodynamically unstable). Figures 8a,b show that the MSD for Li^+ in the cubic phase (Figure 8a) is much larger than in the orthorhombic phase at the same temperature (Figure 8b).

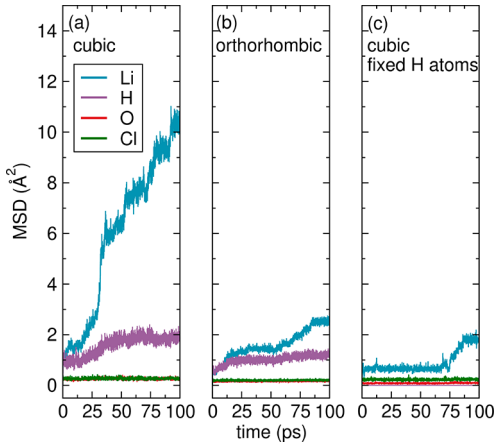

Figure 8. Mean-squared displacement (MSD) of species in (a) cubic, (b) orthorhombic, and (c) cubic (with fixed H) phases at 550 K, evaluated from ionic trajectories calculated over 100 ps AIMD. In (c), motions of O atoms were not fixed.

https://dx.doi.org/10.1021/acs.chemmater.0c02602
Chem. Mater. 2020, 32, 8481−8491

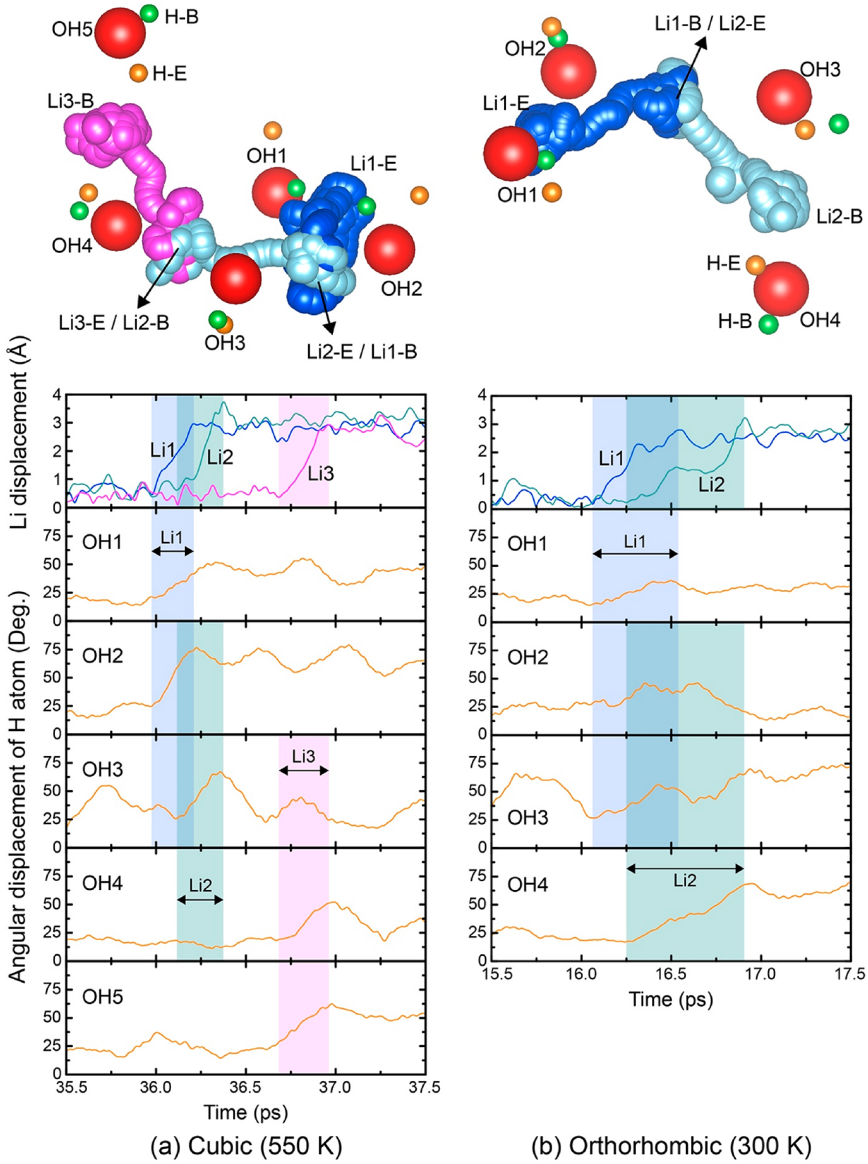

Figure 9. Concerted migration of Li^+ in (a) cubic Li_2OHCl at 550 K and (b) orthorhombic Li_2OHCl at 300 K. Top: trajectories of Li atoms (Li1, blue; Li2, light blue; Li3, pink). The initial and final positions of these ions before and after the migration event are labeled "-B" and "-E", and those of H atoms are also shown (green and orange, respectively). OH groups adjacent to migrating Li ions are labeled as OH1 to OH5. Bottom: translational displacement of Li and angular displacements H as a function of time during the Li migration event. The time span associated with the migration of each Li^+ is shaded; this shading is also replicated in the OH^- displacement plots for those OH adjacent to a migrating Li^+. The angular displacements of OH^- were evaluated by using a moving (box) average over a 200 fs window.

Similarly, the MSD for H atoms in cubic Li_2OHCl (Figure 8a) is about twice as large as in the orthorhombic polymorph (Figure 8b). Taken together, these data imply that the cubic Li_2OHCl phase will exhibit both higher Li^+ mobility and larger H displacements compared to the orthorhombic phase. However, compared to the relatively large displacement of Li^+, the displacements of O, H, and Cl atoms are all relatively small.[14] This indicates that the ionic conductivity measured in experiments is primarily due to Li^+ mobility, not H^+; that is, the antiperovskite is a single-ion conductor.

The relationship between H displacements and Li^+ mobility was further investigated by conducting a constrained AIMD simulation for the cubic phase wherein the H atom positions were fixed. The MSD data for this scenario (Figure 8c) reveal that the Li^+ displacements are severely suppressed when the H dynamics are turned off. Indeed, by comparison of Figure 8b to Figure 8c, it is clear that the Li^+ MSD in the presence of fixed H is even smaller than in the orthorhombic phase. Consequently, the dynamics of the H atoms unequivocally impact Li^+ mobility in cubic Li_2OHCl.

The aforementioned results imply that H^+ rotational and Li^+ translational motions are correlated, as previously discussed by Dawson et al.[22] and Song et al.[19] However, here we can further resolve with AIMD the cooperative motion of multiple Li^+ ions with simultaneous rotational displacements of H about oxygen, in both the orthorhombic structure at room temperature and in the cubic structure at 550 K. Figure 9a shows an example of Li^+ migration in cubic Li_2OHCl, wherein three neighboring Li atoms and five adjacent H atoms move in a concerted fashion (see Video S1, where Li = blue and O = red; H: light pink in the video). Here, two OH anions (identified in Figure 9a as OH1 and OH2) undergo large, quasi-permanent angular

https://dx.doi.org/10.1021/acs.chemmater.0c02602
Chem. Mater. 2020, 32, 8481−8491

displacements (30.5° and 51.9°, respectively) in concert with the motion of Li1 (2.49 Å displacement), as the latter migrates to a vacant site between OH1 and OH2. Before the migration of Li1 completes, Li2 starts its migration toward the newly vacant site previously occupied by Li1 (3.10 Å displacement). Meanwhile, OH3 rotates simultaneously with Li2 migration (41.1° angular displacement). Subsequently, Li3 hops to Li2's original site (2.56 Å displacement), while OH4 and OH5 undergo angular displacements (33.5° and 38.3°, respectively) that track the motion of Li3. These data indicate that the translational displacements of Li atoms are strongly correlated in space and in time to the rotational motions of H atoms in OH bonds, i.e., a "paddlewheel" effect.[23] Similar behavior combining the migration of multiple Li^+ ions with rotational displacements of neighboring anions was recently observed in other solid electrolytes.[38,39]

The migration pathway discussed above involves Li^+ migration between face sites, without a significant contribution from occupancy of edge sites. However, AIMD simulations performed on the cubic phase at a higher temperature of 1000 K, above the experimental melting point ($T_m \approx 573$ K) and therefore where the crystalline phase is metastable shows another migration pathway that passes through the edge site. Video S2 (Li = blue; O = red; H: light pink; Cl = brown) demonstrates such a process. Here, a Li ion on the left side of the image migrates to a vacant site (identified as the space between two O atoms on the right side of the figure) via an edge site (identified as the space between Cl atoms). Compared to the vertex-to-vertex hops discussed above that follow the edges of Li pseudo-octahedra, the face−edge−face hop is a longer distance processes wherein the hopping distance is equal to a lattice constant. These data suggest that at least two different vacancy migration mechanisms could exist in vacancy-rich cubic antiperovskites like Li_2OHCl.

Despite its lower conductivity, the low-temperature orthorhombic phase also exhibits correlations between Li^+ and H^+ dynamics at 300 K. Figure 9b and Video S3 (Li = blue; O = red; H: light pink) illustrate an example migration event in which Li1 and Li2 undergo concerted motion (2.62 and 2.98 Å displacements, respectively), with Li2 migration partially overlapping in time with that of Li1. The end point of the migration of Li2 is at the original Li1 site, the latter site becoming vacant following the migration of Li1. During this process, OH1 and OH2 undergo angular displacements (20.5° and 20.7°, respectively) that track with Li1 migration. Similarly, the orientations of OH2, OH3, and OH4 are altered during the migration of Li2 (angular displacements of 32.7°, 43.2°, and 51.2°, respectively, and 2.98 Å displacement of Li2). The degree of OH angular displacement in the low-temperature orthorhombic structure is similar to that in the high-temperature cubic structure; for example, OH4 in Figure 9b undergoes a large angular displacement similar to that of OH2 in Figure 9a. It implies that these phases have the same degree of correlation between H^+ and Li^+ motions, and the difference in MSD (as shown in Figure 8) originates from the degree of Li^+ and H^+ liberation. This example suggests that the paddlewheel effect can also occur in antiperovskites at low temperatures, similar to what was reported in glassy $75Li_2S-25P_2S_5$[38] at room temperature.

Finally, the present system has a structural analogue in the Na_3OI/Na_2OHI antiperovskites, where unlike Li_3OCl, the fully sodiated end member Na_3OI is stable.[40] The ionic conductivity is about 10^2 higher at the same temperature in Na-deficient Na_2OHI than in Na_3OI (Figure S7), which likely reflects a difference in conduction mechanism as elucidated here.

■ CONCLUSIONS

To understand the relationship between crystal chemistry, atomistic disorder, and ionic conductivity in Li_2OHCl as a model defective antiperovskite ionic conductor, we have performed X-ray, neutron, and electrical conductivity measurements over the temperature range 20−200 °C as well as *ab initio* molecular dynamics (AIMD) simulations at several temperatures. For the first time, we reliably identify the detailed structure, especially the distribution of H, in Li_2OHCl at both low and high temperatures. Significant positional disorder is found for every atom except for chlorine. At temperatures below 311 K (≈38 °C), where the orthorhombic antiperovskite phase is stable, H motion is limited to a plane around O. Above 313 K (≈40 °C), where the cubic antiperovskite phase is stable, a multitude of distinct H positions around the O creates a lobed spherical distribution. Whereas pathways are found for long-range diffusion of the Li ions, H remains chemically bonded to O, forming an unchanging hydroxide anion, which mitigates against a substantial contribution of proton conductivity to the total ionic conductivity. QENS shows that the MSD of OH^- increases with increasing temperature once the cubic phase is stabilized. AIMD confirms these features, and in particular, simulations in which the OH^- rotation is "turned off", Li^+ MSD is dramatically reduced. Thus, we find conclusive evidence for a "paddlewheel" mechanism of ion conduction in this defective antiperovskite structure. The present results suggest that to achieve high ionic conductivity in antiperovskites, both a high cation vacancy concentration and the presence of an octahedral anion with rotational disorder are beneficial.

■ ASSOCIATED CONTENT

Supporting Information

The Supporting Information is available free of charge at https://pubs.acs.org/doi/10.1021/acs.chemmater.0c02602.

Temperature dependence of ionic conductivity and differential scanning calorimetry (DSC) analysis for Li_2OHCl, Rietveld refinement of X-ray diffraction for Li_2OHCl at 373 and 300 K zoomed in at a representative Q range, Rietveld refinement of neutron diffraction for Li_2OHCl at 298 K acquired from POWGEN (ORNL), and X-ray pair distribution function (PDF) of Li_2OHCl from 100 to 370 K (PDF)

Movie S1 (MP4)

Movie S2 (MP4)

Movie S3 (MP4)

■ AUTHOR INFORMATION

Corresponding Author

Yet-Ming Chiang − *Massachusetts Institute of Technology, Cambridge, Massachusetts 02139, United States;* orcid.org/0000-0002-0833-7674; Email: ychiang@mit.edu

Authors

Fei Wang − *Massachusetts Institute of Technology, Cambridge, Massachusetts 02139, United States;* orcid.org/0000-0002-2057-5130

https://dx.doi.org/10.1021/acs.chemmater.0c02602
Chem. Mater. 2020, 32, 8481−8491

Hayden A. Evans − *Center for Neutron Research, National Institute of Standards and Technology, Gaithersburg, Maryland 20899, United States;* orcid.org/0000-0002-1331-4274
Kwangnam Kim − *University of Michigan, Ann Arbor, Michigan 48109, United States;* orcid.org/0000-0003-1149-1733
Liang Yin − *Argonne National Laboratory, Lemont, Illinois 60439, United States;* orcid.org/0000-0001-5396-782X
Yiliang Li − *Massachusetts Institute of Technology, Cambridge, Massachusetts 02139, United States*
Ping-Chun Tsai − *Massachusetts Institute of Technology, Cambridge, Massachusetts 02139, United States*
Jue Liu − *Oak Ridge National Laboratory, Oak Ridge, Tennessee 37831, United States;* orcid.org/0000-0002-4453-910X
Saul H. Lapidus − *Argonne National Laboratory, Lemont, Illinois 60439, United States;* orcid.org/0000-0002-7486-4325
Craig M. Brown − *Center for Neutron Research, National Institute of Standards and Technology, Gaithersburg, Maryland 20899, United States*
Donald J. Siegel − *University of Michigan, Ann Arbor, Michigan 48109, United States;* orcid.org/0000-0001-7913-2513

Complete contact information is available at:
https://pubs.acs.org/10.1021/acs.chemmater.0c02602

Author Contributions

F.W., H.A.E., and K.K. contributed equally to this work.

Notes

The authors declare no competing financial interest.

■ ACKNOWLEDGMENTS

This work was supported as part of the Joint Center for Energy Storage Research, an Energy Innovation Hub funded by the U.S. Department of Energy, Office of Science, Basic Energy Sciences. H.A.E. thanks the National Research Council (USA) for financial support through the Research Associate Program. This work made use of the MRL Materials Research Science and Engineering Center (MRSEC) Shared Experimental Facilities at MIT, supported by the National Science Foundation under Award DMR-1419807. Certain commercial equipment, instruments, or materials are identified in this document. Such identification does not imply recommendation or endorsement by the National Institute of Standards and Technology, nor does it imply that the products identified are necessarily the best available for the purpose.

■ REFERENCES

(1) Janek, J.; Zeier, W. G. A Solid Future for Battery Development. *Nat. Energy* **2016**, *1*, 1−4.
(2) Manthiram, A.; Yu, X.; Wang, S. Lithium Battery Chemistries Enabled by Solid-State Electrolytes. *Nat. Rev. Mater.* **2017**, *2*, 1−16.
(3) Zhao, Y.; Daemen, L. L. Superionic Conductivity in Lithium-Rich Anti-perovskites. *J. Am. Chem. Soc.* **2012**, *134*, 15042−15047.
(4) Lu, Z.; Chen, C.; Baiyee, Z. M.; Chen, X.; Niu, C.; Ciucci, F. Defect Chemistry and Lithium Transport in Li_3OCl Anti-perovskite Superionic Conductors. *Phys. Chem. Chem. Phys.* **2015**, *17*, 32547−32555.
(5) Stegmaier, S.; Voss, J.; Reuter, K.; Luntz, A. C. Li^+ Defects in a Solid-state Li Ion Battery: Theoretical Insights with a Li_3OCl Electrolyte. *Chem. Mater.* **2017**, *29*, 4330−4340.
(6) Chiang, Y.-M.; Birnie, D. P.; Kingery, W. D. *Physical Ceramics*; J. Wiley: New York, 1997.
(7) Ye, Z.-G. *Handbook of Advanced Dielectric, Piezoelectric and Ferroelectric Materials: Synthesis, Properties and Applications*; Elsevier: 2008.
(8) Snaith, H. J. Present Status and Future Prospects of Perovskite Photovoltaics. *Nat. Mater.* **2018**, *17*, 372−376.
(9) Kim, K.; Siegel, D. J. Correlating Lattice Distortions, Ion Migration Barriers, and Stability in Solid Electrolytes. *J. Mater. Chem. A* **2019**, *7*, 3216−3227.
(10) Hood, Z. D.; Wang, H.; Samuthira Pandian, A.; Keum, J. K.; Liang, C. Li_2OHCl Crystalline Electrolyte for Stable Metallic Lithium Anodes. *J. Am. Chem. Soc.* **2016**, *138*, 1768−1771.
(11) Zhang, J.; Han, J.; Zhu, J.; Lin, Z.; Braga, M. H.; Daemen, L. L.; Wang, L.; Zhao, Y. High Pressure-High Temperature Synthesis of Lithium-rich $Li_3O(Cl, Br)$ and $Li_{3-x}Ca_{x/2}OCl$ Anti-perovskite Halides. *Inorg. Chem. Commun.* **2014**, *48*, 140−143.
(12) Braga, M. H.; Murchison, A. J.; Ferreira, J. A.; Singh, P.; Goodenough, J. B. Glass-Amorphous Alkali-Ion Solid Electrolytes and their Performance in Symmetrical Cells. *Energy Environ. Sci.* **2016**, *9*, 948−954.
(13) Hanghofer, I.; Redhammer, G. J.; Rohde, S.; Hanzu, I.; Senyshyn, A.; Wilkening, H. M. R.; Rettenwander, D. Untangling the Structure and Dynamics of Lithium-Rich Anti-perovskites Envisaged as Solid Electrolytes for Batteries. *Chem. Mater.* **2018**, *30*, 8134−8144.
(14) Song, A. Y.; Turcheniuk, K.; Leisen, J.; Xiao, Y.; Meda, L.; Borodin, O.; Yushin, G. Understanding Li-Ion Dynamics in Lithium Hydroxychloride (Li_2OHCl) Solid State Electrolyte via Addressing the Role of Protons. *Adv. Energy Mater.* **2020**, *10*, 1903480.
(15) Li, Y.; Zhou, W.; Xin, S.; Li, S.; Zhu, J.; Lu, X.; Cui, Z.; Jia, Q.; Zhou, J.; Zhao, Y.; Goodenough, J. B. Fluorine-doped Antiperovskite Electrolyte for All-Solid-State Lithium-Ion Batteries. *Angew. Chem., Int. Ed.* **2016**, *55*, 9965−9968.
(16) Zhang, Y.; Zhao, Y.; Chen, C. Ab Initio Study of the Stabilities of and Mechanism of Superionic Transport in Lithium-Rich Antiperovskites. *Phys. Rev. B: Condens. Matter Mater. Phys.* **2013**, *87*, 134303.
(17) Emly, A.; Kioupakis, E.; Van der Ven, A. Phase Stability and Transport Mechanisms in Antiperovskite Li_3OCl and Li_3OBr Superionic Conductors. *Chem. Mater.* **2013**, *25*, 4663−4670.
(18) Schwering, G.; Hönnerscheid, A.; van Wüllen, L.; Jansen, M. High Lithium Ionic Conductivity in the Lithium Halide Hydrates Li_{3-n} (OH_n) Cl ($0.83 \leq n \leq 2$) and Li_{3-n} (OH_n) Br ($1 \leq n \leq 2$) at Ambient Temperatures. *ChemPhysChem* **2003**, *4*, 343−348.
(19) Song, A.-Y.; Xiao, Y.; Turcheniuk, K.; Upadhya, P.; Ramanujapuram, A.; Benson, J.; Magasinski, A.; Olguin, M.; Meda, L.; Borodin, O.; Yushin, G. Protons Enhance Conductivities in Lithium Halide Hydroxide/Lithium Oxyhalide Solid Electrolytes by Forming Rotating Hydroxy Groups. *Adv. Energy. Mater.* **2018**, *8*, 1700971.
(20) Koedtruad, A.; Patino, M. A.; Ichikawa, N.; Kan, D.; Shimakawa, Y. Crystal Structures and Ionic Conductivity in Li_2OHX (X= Cl, Br) Antiperovskites. *J. Solid State Chem.* **2020**, *286*, 121263.
(21) Howard, J.; Hood, Z. D.; Holzwarth, N. A. W. Fundamental Aspects of the Structural and Electrolyte Properties of Li_2OHCl from Simulations and Experiment. *Phys. Rev. Mater.* **2017**, *1*, 075406.
(22) Dawson, J. A.; Attari, T. S.; Chen, H.; Emge, S. P.; Johnston, K. E.; Islam, M. S. Elucidating Lithium-Ion and Proton Dynamics in Anti-perovskite Solid Electrolytes. *Energy Environ. Sci.* **2018**, *11*, 2993−3002.
(23) Jansen, M. Volume Effect or Paddle-Wheel Mechanism—Fast Alkali-Metal Ionic Conduction in Solids with Rotationally Disordered Complex Anions. *Angew. Chem., Int. Ed. Engl.* **1991**, *30*, 1547−1558.
(24) Eilbracht, C.; Kockelmann, W.; Hohlwein, D.; Jacobs, H. Orientational Disorder in Perovskite like Structures of Li_2X (OD)(X = Cl, Br) and LiBr· D_2O. *Phys. B* **1997**, *234*, 48−50.
(25) Coelho, A. A. TOPAS-Academic: An Optimization Program Integrating Computer Algebra and Crystallographic Objects Written in C++. *J. Appl. Crystallogr.* **2018**, *51*, 210−218.

(26) Pawley, G. Unit-cell Refinement from Powder Diffraction Scans. *J. Appl. Crystallogr.* **1981**, *14*, 357−361.
(27) Momma, K.; Ikeda, T.; Belik, A. A.; Izumi, F. Dysnomia, A Computer Program for Maximum-Entropy Method (MEM) Analysis and Its Performance in the MEM-based Pattern Fitting. *Powder Diffr.* **2013**, *28*, 184−193.
(28) Izumi, F.; Ikeda, T. A Rietveld-Analysis Programm RIETAN-98 and its Applications to Zeolites. *Mater. Sci. Forum* **2000**, *321−324*, 198−205.
(29) Izumi, F.; Momma, K. Three-Dimensional Visualization in Powder Diffraction. *Solid State Phenom.* **2007**, *130*, 15−20.
(30) Toby, B. H.; Von Dreele, R. B. GSAS-II: the Genesis of a Modern Open-Source All Purpose Crystallography Software Package. *J. Appl. Crystallogr.* **2013**, *46*, 544−549.
(31) Farrow, C.; Juhas, P.; Liu, J.; Bryndin, D.; Božin, E.; Bloch, J.; Proffen, T.; Billinge, S. PDFfit2 and PDFgui: Computer Programs for Studying Nanostructure in Crystals. *J. Phys.: Condens. Matter* **2007**, *19* (33), 335219.
(32) Kresse, G.; Furthmüller, J. Efficient Iterative Cchemes for Ab Initio Total-Energy Calculations using a Plane-Wave Basis Set. *Phys. Rev. B: Condens. Matter Mater. Phys.* **1996**, *54*, 11169.
(33) Perdew, J. P.; Burke, K.; Ernzerhof, M. Generalized Gradient Approximation Made Simple. *Phys. Rev. Lett.* **1996**, *77*, 3865.
(34) Blöchl, P. E. Projector Augmented-Wave Method. *Phys. Rev. B: Condens. Matter Mater. Phys.* **1994**, *50*, 17953.
(35) Kresse, G.; Joubert, D. From Ultrasoft Pseudopotentials to the Projector Augmented-Wave Method. *Phys. Rev. B: Condens. Matter Mater. Phys.* **1999**, *59*, 1758.
(36) Wang, Y.; Richards, W. D.; Ong, S. P.; Miara, L. J.; Kim, J. C.; Mo, Y.; Ceder, G. Design Principles for Solid-State Lithium Superionic Conductors. *Nat. Mater.* **2015**, *14*, 1026−1031.
(37) Dawson, J. A.; Canepa, P.; Famprikis, T.; Masquelier, C.; Islam, M. S. Atomic-Scale Influence of Grain Boundaries on Li-Ion Conduction in Solid Electrolytes for All-Solid-State Batteries. *J. Am. Chem. Soc.* **2018**, *140*, 362−368.
(38) Zhang, Z.; Roy, P.-N.; Li, H.; Avdeev, M.; Nazar, L. F. Coupled Cation−Anion Dynamics Enhances Cation Mobility in Room-Temperature Superionic Solid-State Electrolytes. *J. Am. Chem. Soc.* **2019**, *141*, 19360−19372.
(39) Smith, J. G.; Siegel, D. J. Low-Temperature Paddlewheel Effect in Glassy Solid Electrolytes. *Nat. Commun.* **2020**, *11*, 1−11.
(40) Zhu, J.; Wang, Y.; Li, S.; Howard, J. W.; Neuefeind, J.; Ren, Y.; Wang, H.; Liang, C.; Yang, W.; Zou, R.; Jin, C.; Zhao, Y. Sodium Ion Transport Mechanisms in Antiperovskite Electrolytes Na_3OBr and Na_4OI_2: An in Situ Neutron Diffraction Study. *Inorg. Chem.* **2016**, *55* (12), 5993−5998.

https://dx.doi.org/10.1021/acs.chemmater.0c02602
Chem. Mater. 2020, 32, 8481−8491